Seismic signatures of partial steam saturation in fractured geothermal reservoirs: insights from poroelasticity

Gabriel E. Quiroga[1], J. Germán Rubino[2], Santiago G. Solazzi[1], Nicolás D. Barbosa[1], Marco Favino[1], and Klaus Holliger[1]

Running head: *Seismic signatures of steam*

[1] Institute of Earth Sciences, University of Lausanne, Lausanne, Switzerland.

[2] CONICET, Centro Atómico Bariloche - CNEA, San Carlos de Bariloche, Argentina.

ABSTRACT

Detecting the presence of gaseous formation fluids, estimating the respective volumes, and characterizing their spatial distribution is important for a wide range of applications, notably for geothermal energy production. The ability to obtain such information from remote geophysical measurements constitutes a fundamental challenge, which needs to be overcome to address a wide range of problems, such as the estimation of the reservoir temperature and pressure conditions. With these motivations, we compute the body wave velocities of a fractured granitic geothermal reservoir formation with varying quantities of steam to analyze the seismic signatures in a partial saturation context. We employ a poroelastic upscaling approach that accounts for mesoscale fluid pressure diffusion (FPD) effects induced by the seismic strain field, and, thus, describes the governing physical processes more accurately than standard representations. Changes in seismic velocities due to steam saturation are compared with changes associated with fracture density variations, as both are plausible results of pressure changes in geothermal reservoirs. We find that steam saturation has a significant impact on P-wave velocities while affecting S-wave velocities to a significantly lesser extent. This contrasting behavior allows to discriminate between fracture density and steam saturation changes by means of P- and S-wave velocity ratio analyses. To evaluate the potential of seismic methods to provide this information, a canonical geothermal reservoir model is employed to compute Rayleigh wave velocity dispersion and seismic reflection amplitude vs angle (AVA) curves. These studies reveal that AVA analyses allow to differentiate changes in fracture density

from changes in steam saturation. We also note that Rayleigh-wave-based techniques are much less sensitive to steam content changes than to fracture density changes. Comparisons with elastic approaches show that including FPD effects through the use of a poroelastic model is crucial for the reliable detection and characterization of steam in fractured geothermal reservoirs.

INTRODUCTION

The remote detection and characterization of the presence of gaseous phases in fractured geological formations is essential for numerous applications of economic and environmental importance, such as, for example, the monitoring of CO_2 sequestration projects or the identification of gas pockets in hydrocarbon reservoirs (e.g., Fatti et al., 1994; Kazemeini et al., 2010; Roach et al., 2015; Stork et al., 2018). In particular, the detection of the presence or absence of steam in high-enthalpy geothermal reservoirs can provide unique insights with regard to the system's temperature and pressure conditions (e.g., Scott, 2020). Most high-enthalpy geothermal reservoirs are associated with fractured environments. Open fractures are weak and permeable features that tend to constitute preferential pathways for fluid flow and, thus, greatly affect the overall hydraulic and mechanical properties of the medium. Correspondingly, seismic methods are extensively used for the characterization and monitoring of geothermal projects (e.g., Gunasekera et al., 2003; Obermann et al., 2015; Taira et al., 2018; Sánchez-Pastor et al., 2021; Toledo et al., 2022).

Fractures prevail over a wide range of scales (e.g., Vermilye and Scholz, 1995; Bonnet et al., 2001), from the regional scale all the way to the microscopic one. Seismic waves travelling through fractured media tend to experience an increase in attenuation, dispersion, and scattering as well as a general decrease in the overall propagation velocity. The relative scale of the fractures with respect to the prevailing seismic wavelengths determines which physical mechanisms dominate. Mesoscale fractures, which are the focus of this study, are much smaller than the prevailing wavelengths, but much larger than the pore scale. Fractures in this scale range do not promote significant scattering and are well below the explicit resolution of seismic exploration techniques, but they do manifest themselves through pronounced increases of attenuation and dispersion. Given the seemingly universal hyperbolic distribution of fracture lengths (e.g., de Dreuzy et al., 2001; Bonnet et al., 2001), mesoscale fractures tend to be particularly abundant and play a correspondingly important role with regard to the effective hidraulic properties of fractured reservoirs. When a seismic wave travels through a formation containing mesoscale fractures, pore fluid pressure gradients arise between the softer fractures and the stiffer embedding background as well as between interconnected fractures (e.g., Rubino et al., 2013, 2014, 2016; Vinci et al., 2014; Gurevich et al., 2009). These pressure imbalances cause fluid pressure diffusion (FPD) between the fractures and their embedding background known as fracture-to-background FPD, as well as between connected fractures, known as fracture-to-fracture FPD. The corresponding effects manifest themselves in the form of seismic attenuation and velocity dispersion. The governing physical processes can be assessed using Biot's (1962) theory of poroelasticity, which permits to comprehensively characterize FPD effects induced by the strains associated with seismic waves. However, the numerical simulation of wave propagation accounting for the effects of mesoscale fractures on seismic attenuation and dispersion is computationally prohibitive, due to the very fact that the scale, at which these effects prevail, is much smaller than the seismic wavelengths (e.g., Rubino et al., 2016). To circumvent this problem, effective-medium-type upscaling approaches have proven to be an efficient means of characterizing FPD effects in formations containing mesoscale heterogeneities and/or fractures.

In the context of effective-medium-type upscaling approaches, a representative sample of the formation of interest is subjected to a series of numerical stress or displacement tests in order to emulate the deformation imposed by a propagating seismic wavefield (e.g., Masson and Pride, 2007; Rubino et al., 2009). The resulting stress and strain fields are then used to infer the equivalent phase velocity and attenuation for the medium. In the recent past, these upscaling approaches have been successfully employed to explore FPD effects in mesoscale fractured media of increasing complexity and realism (e.g., Rubino et al., 2013, 2017; Hunziker et al., 2018). Most of the above mentioned works were, however, based on the assumption of full water saturation. Conversely, in high-enthalpy geothermal systems, it is important to assess the effects of partial saturation, as steam may be present due to natural causes (e.g., Scott, 2020) or due to decompression effects during production operations (e.g., Barbier, 2002).

The presence of steam in geothermal reservoirs is governed by the local pressure and temperature conditions, and, thus, it is of interest to assess whether seismic methods can provide relevant information in this regard. Grab et al. (2017) studied the seismic effects of partial steam saturation in a fractured geothermal reservoir. To do so, the authors considered that the steam phase is distributed in the form of sub-pore-scale bubbles throughout primarily water-saturated fractures and their embedding background. As such, the authors represent the properties of the corresponding gas-liquid mixture as an effective fluid for the purposes of modelling. There is, however, evidence to show that the spatial distribution of wetting and non-wetting fluids, such as water and steam, in fractured formations is partly determined by capillary forces (e.g., Glass et al., 2004). This characteristic, in turn, implies that steam should preferentially concentrate in fractures, as they constitute regions with particularly low entry pressures. Taking this fluid distribution characteristic into account, Solazzi et al. (2020) analyzed the effects of fracture-to-background and fracture-to-fracture FPD processes in a brine- and CO_2-saturated fractured formation. The authors show that the amount and the spatial distribution of the fluid phases have a significant effect on seismic velocity and attenuation estimates for both P- and S-waves. Conversely, the importance of these effects in scenarios with varying fracture densities and connectivities, which have been identified as key variables with regard to the seismic response of monosaturated media, remains as of yet unexplored.

The objective of this study is to improve our understanding of the seismic response of partially saturated fractured media in general and high-enthalpy fractured geothermal reservoirs in particular. To this end, we focus on the presence or absence of steam in high-enthalpy fractured geothermal reservoirs and explore the corresponding impact on seismic characterization and monitoring efforts. Throughout this study, changes in seismic velocities due to steam saturation are compared with changes associated with pure fracture density variations, as both saturation and fracture density changes are plausible results of pressure changes in geothermal reservoirs. The paper proceeds as follows. First, we present the methodological background related to the generation of poroelastic models of partially saturated fractured media and for evaluating their effective seismic properties by accounting for the prevailing FPD effects. Then, we analyze the resulting behavior of P- and S-wave velocities as functions of the steam saturation of the fractures and their interconnectivity degree. These results are compared to those corresponding to the high-frequency limit, which does not account for FPD effects. Based on these results, we then consider a canonical geological model and study the sensitivity of Rayleigh waves and variations of seismic reflection amplitudes with incidence angle (AVA) with regard to these parameters. As previously mentioned, we also explore whether time-lapse seismic monitoring has the potential of differentiating between changes in fracture density and steam saturation.

METHODOLOGY

In this section, we provide a summary of the numerical upscaling procedure employed to obtain effective seismic properties of poroelastic samples containing mesoscale fractures. We then describe how we generate realistic fracture networks with different levels of fracture interconnectivity and varying fracture fluid content. Finally, we provide an overview of FPD effects in fractured media and their impact on key seismic characteristics.

Numerical Upscaling Procedure

To obtain effective seismic properties of a porous medium containing mesoscale fractures, we consider a typical sample of the corresponding medium and subject it to a set of numerical tests consisting of harmonic displacements applied on its boundaries (e.g., Rubino et al., 2009). The response of the samples are evaluated using Biot's theory of poroelasticity, which naturally accounts for FPD effects (Biot, 1956a,b). The rock samples contain mesoscopic fractures that are conceptualized as highly porous, highly permeable, and highly compliant inclusions embedded in a much stiffer and much less porous and permeable background (e.g., Nakagawa and Schoenberg, 2007). It is worth noting that, even in presence of media with very low porosities and permeabilities, the theory of poroelasticity remains valid and that, for sufficiently low values of these properties, the medium effectively behaves as an elastic solid (e.g., Bourbié et al., 1987; He et al., 2022). For seismic frequencies, it is safe to neglect inertial terms in the numerical upscaling procedure (e.g., Rubino et al., 2013). Hence, the poroelastic equations of motion (Biot, 1956a,b) reduce to the so-called consolidation equations (Biot, 1941), which, in the so-called $\boldsymbol{u} - p$ form and in the space-frequency domain are given by

$$\nabla \cdot \boldsymbol{\sigma} = 0, \tag{1}$$

$$-j\alpha\nabla \cdot \boldsymbol{u}(\omega) - j\frac{p(\omega)}{M} + \frac{1}{\omega}\nabla \cdot (\frac{k}{\eta}\nabla p(\omega)) = 0, \tag{2}$$

where $\boldsymbol{\sigma}$ is the total stress tensor, ω the angular frequency, j the imaginary unit, $\boldsymbol{u}$ is the solid displacement, p the fluid pressure, η the fluid viscosity, κ the permeability, M the fluid storage coefficient, and α the Biot-Willis parameter. The total stress tensor $\boldsymbol{\sigma}$ is a function of the strain $\boldsymbol{\epsilon}$ and of the fluid pressure p and can be written as

$$\boldsymbol{\sigma} = 2\mu\boldsymbol{\epsilon}(\boldsymbol{u}) + \lambda_c \mathrm{tr}(\boldsymbol{\epsilon}(\mathbf{u}))\boldsymbol{I} - \alpha p \boldsymbol{I}, \tag{3}$$

with $\boldsymbol{\epsilon}(\boldsymbol{u})$ defined as

$$\boldsymbol{\epsilon}(\boldsymbol{u}) = \frac{\nabla \boldsymbol{u} + \nabla \boldsymbol{u}^T}{2}, \tag{4}$$

where μ is the shear modulus of the dry frame, λ_c the Lamé parameter, $\mathbf{I}$ is the identity matrix, and tr() denotes the trace operator. The Biot-Willis parameter α, the fluid storage coefficient M, and the Lamé parameter λ_c are given by

$$\alpha = 1 - \frac{K_m}{K_s}, \tag{5}$$

$$M = \left(\frac{\alpha - \phi}{K_s} + \frac{\phi}{K_f}\right)^{-1}, \tag{6}$$

and

$$\lambda_c = K_m + \alpha^2 M - \frac{2}{3}\mu, \tag{7}$$

where ϕ denotes the porosity and K_f, K_m, and K_s are the bulk moduli of the fluid phase, the dry matrix, and the solid grains, respectively.

Due to computational constraints, we perform a 2D analysis under the hypothesis of plane strain conditions (Rubino et al., 2016). As previously stated, in order to obtain the effective stiffness matrix of the considered medium, we apply three oscillatory relaxation tests to a representative sample (Rubino et al., 2016). The first test (Figure 1a) consists of a harmonic vertical compression, which is performed by applying a time-harmonic homogeneous vertical displacement at the top boundary of the representative sample, while keeping the vertical displacement null at the bottom boundary. The second test (Figure 1b) is a harmonic horizontal compression test, which consists of the application of a normal displacement at a lateral boundary of the sample, while keeping the horizontal displacement null at the opposing boundary. The third and final test (Figure 1c) consists of the application of a harmonic horizontal displacement at the top boundary of the sample, while keeping the bottom boundary fixed in place. Following Favino et al. (2020), unless otherwise stated, the displacements and pressures obey periodic boundary conditions. Given that the overall response of a heterogeneous poroelastic medium can be effectively reproduced by those of an effective homogeneous viscoelastic solid (e.g., Rubino et al., 2016; Solazzi et al., 2016), the volumetric averages of stress and strain, in response to each of the three tests outlined above, can be related through an effective frequency-dependent and complex-valued stiffness matrix (e.g., Rubino et al., 2016)

$$\begin{pmatrix} \langle \sigma_{11}^k(\omega) \rangle \\ \langle \sigma_{22}^k(\omega) \rangle \\ \langle \sigma_{12}^k(\omega) \rangle \end{pmatrix} = \begin{pmatrix} C_{11}(\omega) & C_{12}(\omega) & C_{16}(\omega) \\ C_{12}(\omega) & C_{22}(\omega) & C_{26}(\omega) \\ C_{16}(\omega) & C_{26}(\omega) & C_{66}(\omega) \end{pmatrix} \begin{pmatrix} \langle \epsilon_{11}^k(\omega) \rangle \\ \langle \epsilon_{22}^k(\omega) \rangle \\ \langle 2\epsilon_{12}^k(\omega) \rangle \end{pmatrix}, \tag{8}$$

where $k = 1, 2, 3$ refers to three oscillatory tests, $C_{ij}(\omega)$ are the components of the stiffness matrix in Voigt notation, and $\langle \epsilon_{ij}^k(\omega) \rangle$ and $\langle \sigma_{ij}^k(\omega) \rangle$ represent the volume-averages of the strain and stress components in response to the test k, respectively. This system of equations has nine equations and six unknowns, and the best-fitting values of $C_{ij}(\omega)$ are obtained by a least squares algorithm, using the averaged stress and strain fields obtained from the three tests for each frequency. The resulting phase velocities are (Rubino et al., 2016):

$$V_{P,S}(\omega, \theta) = \frac{\omega}{\Re(\kappa_{P,S}(\omega, \theta))}, \tag{9}$$

where $\Re$ denotes the real part, $\kappa_{P,S}(\omega, \theta)$ are the complex-valued wavenumbers obtained by solving the elastodynamic equation in a medium defined by the stiffness matrix in Equation (8). The reader is referred to the work of Rubino et al. (2016) for the detailed procedure of obtaining the coefficients of the stiffness matrix combining the stress and strain measurements of the three oscillatory tests and the resulting phase velocities. Further details about the corresponding numerical implementation and boundary conditions can be found in Favino et al. (2020). Effective-medium-type scaling approaches are based on the assumption that the size of the sample modelled constitutes a representative elementary volume (REV) of the probed formation. A sample corresponds to a REV, (i) when it is structurally typical of the studied rock volume and (ii) when the inferred seismic properties are independent of the boundary conditions applied (e.g., Milani et al., 2016; Caspari et al., 2016). When considering complex fracture networks, generating samples of the medium that are large enough to constitute a REV may not be feasible. To overcome this difficulty, we follow the approach of Rubino et al. (2009) and Quiroga et al. (2022), who employ the previously outlined upscaling approach in a Monte Carlo fashion on sub-REV-size samples that are within our numerical capabilities. The Monte Carlo procedure consists of obtaining representative mechanical properties by averaging a sufficient number of stochastic realizations of samples with the same statistical properties. In

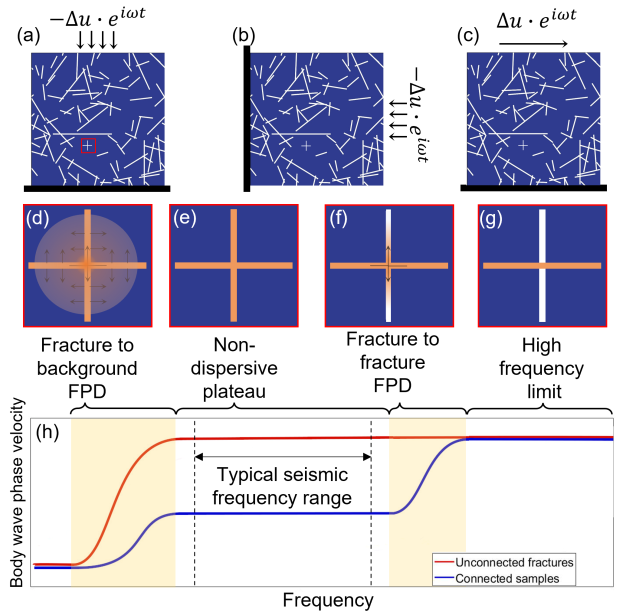

Figure 1: Schematic illustration of the (a) vertical, (b) horizontal, and (c) shear numerical oscillatory relaxation tests employed to obtain the equivalent stiffness matrix of the considered sample. (d, e, f, g) Fluid pressure distributions in a subsection of the sample highlighted in (a) subjected to a vertical compression for different dispersion regimes. Increasing pressure is denoted by progressive intensities of orange. (d) fracture-to-background FPD: pressure exchange between fractures and their embedding background, (e) non-dispersive plateau: pressure is equilibrated between connected fractures; (f) fracture-to-fracture FPD: pressure exchange between connected fractures; (g) High frequency limit: pressure confined to the horizontal fracture. (h) body wave velocities as functions of frequency for samples with unconnected fractures (red line) and connected fractures (blue line). The frequency ranges where body wave dispersion due to fracture-to-background and fracture-to-fracture FPD prevails are highlighted in yellow. Typical frequency range of seismic studies is shown inside the non-dispersive plateau.

this study, we obtain P- and S-wave velocities of samples with the same degree of fracture connectivity and steam saturation. The stabilization of the standard deviation of the averaged velocities as a function of the number of realizations serves as the convergence criterion (Rubino et al., 2009). Once the convergence has been achieved, we can consider the inferred averaged seismic velocities as being representative for the considered formation as a whole. Correspondingly, we refer to these averages as *effective body wave velocities* from now on. Appendix A provides a step-by-step description of the upscaling procedure outlined above.

Fracture network properties

For the numerical analysis, we consider mesoscale fracture networks with a uniform distribution of fracture orientations and a power law distribution of fracture lengths. The latter is widely regarded as a seemingly universal and ubiquitous characteristic of fractures (e.g., de Dreuzy et al., 2001; Bonnet et al., 2001). Following previous works on this topic (e.g., Hunziker et al., 2018; Quiroga et al., 2022), we use

$$n(L) = F_d(a-1)\frac{L^{-a}}{L_{min}^{1-a}}; L \in [L_{min}, L_{max}], \tag{10}$$

where L is the fracture length, $n(L)$, is the density function quantifying the number of fractures in the considered fractured formation with a length comprised between L and $L + dL$, where dL denotes an infinitesimal increment of length, a is the so-called characteristic exponent of the fracture size distribution, and L_{min} and L_{max} are the bounding minimum and maximum length values, respectively. The exponent a can take values between 1.5 and 3 and controls the prevalence of shorter to longer fractures within the limits given by L_{min} and L_{max}. Following Hunziker et al. (2018), we choose an intermediate value of 2.25. F_d is the fracture density defined as the ratio of area of the fractures and the total area of the sample. With regard to the interconnectivity of fractures, we consider three scenarios: (i) a randomly connected scenario, where fractures are randomly placed; (ii) a fully connected scenario, where fractures are randomly placed but ensuring that all of them have at least one connection with another fracture by randomly relocating unconnected fractures; (iii) a fully unconnected scenario, where fractures do not have any connections between each other, a configuration that is achieved by randomly relocating connected fractures.

In order to simulate partial saturation of water and steam in the context of a fractured formation, we use the following saturation procedure. We start with samples whose embedding background and fractures are completely saturated with water. Then, we progressively increase the percentage of steam saturation in the fracture pore space until all fractures are steam saturated, while the background remains saturated with water. We ignore the possibility that some regions of the embedding low-porosity background may also contain steam as the corresponding mechanical effects are of subordinate importance to fracture related FPD effects. Fractures are always completely saturated with either water or steam. This is achieved by saturating first the longer fractures with steam, as they tend to be associated with greater permeabilities (e.g., Vermilye and Scholz, 1995). It is expected that these fractures are more susceptible to pressure changes, which are a key driving mechanism for the appearance of steam in our model. In this context, it is important to note that the poroelastic properties, including the permeability, of the material filling the fractures, are kept invariant in our model in order to minimize secondary effects and focus on those related to changes in saturation and interconnectivity.

In order to minimize the number of samples that ensure convergence of the Monte Carlo procedure, we impose certain restrictions in the fracture network creation process. For each realization to be averaged in the Monte Carlo procedure, we draw a particular sampling of the fracture length distribution by employing the density function described in Equation 10. This fracture length distribution is then used, by varying fracture placement and orientations, to generate the three different connectivity scenarios explained above. These samples are initially considered to be completely saturated with water and their fracture networks are then progressively saturated with steam according to the procedure described above, thus, resulting in samples with varying steam saturation values. In this way, each realization is composed of several samples, which share a common fracture length distribution, and, in the case of samples with a same degree of connectivity, but varying steam saturation, the placement and orientation of fractures is identical. This is illustrated in Figure 2, which illustrates that the saturation process is done on the same fracture network for each connectivity scenario. For each new realization to be averaged, a new fracture length distribution is drawn, and the process is repeated until the convergence criterion for each connectivity and steam saturation scenario is achieved. Like this, we can assure that changes in the mechanical properties in each realization are either due to changes in fracture connectivity or due to changes in saturation and, hence, unrelated to other factors, which are not the objective of study of this work.

Fluid Pressure Diffusion Effects

In the following, we briefly outline the nature and characteristics of FPD effects in fractured formations, based on recent works in the literature (e.g., Rubino et al., 2013, 2017; Hunziker et al., 2018; Solazzi et al., 2020). We consider samples with fractures that are in the mesoscopic scale range, that is, the fractures are larger than the pore scale but smaller than the dominant wavelength. For typical seismic frequencies between 5 and 60 Hz, and typical upper crustal P-wave velocities between 3000 and 6000 m/s, the wavelengths tend to be larger than 50 m, while the fractures considered in these studies tend to be shorter than one meter. When a seismic wave propagates through a fluid-saturated porous medium containing fractures in this scale range, the viscous friction associated with FPD effects results in seismic energy dissipation, which manifests itself in the form of velocity dispersion and attenuation. In the presence of connected fractures, two manifestations of FPD can arise (Rubino et al., 2013). The large stiffness contrast between fractures and their embedding background generates pressure gradients in response to the strains associated with seismic wave propagation, which, in turn, generate oscillatory fluid flow between these regions. This process is referred to as fracture-to-background FPD (Figure 1d). Additionally, fluid pressure gradients occurring within intersecting fractures undergoing different levels of compression/extension due to their respective orientations with respect to the direction of seismic wave propagation result in fracture-to-fracture FPD

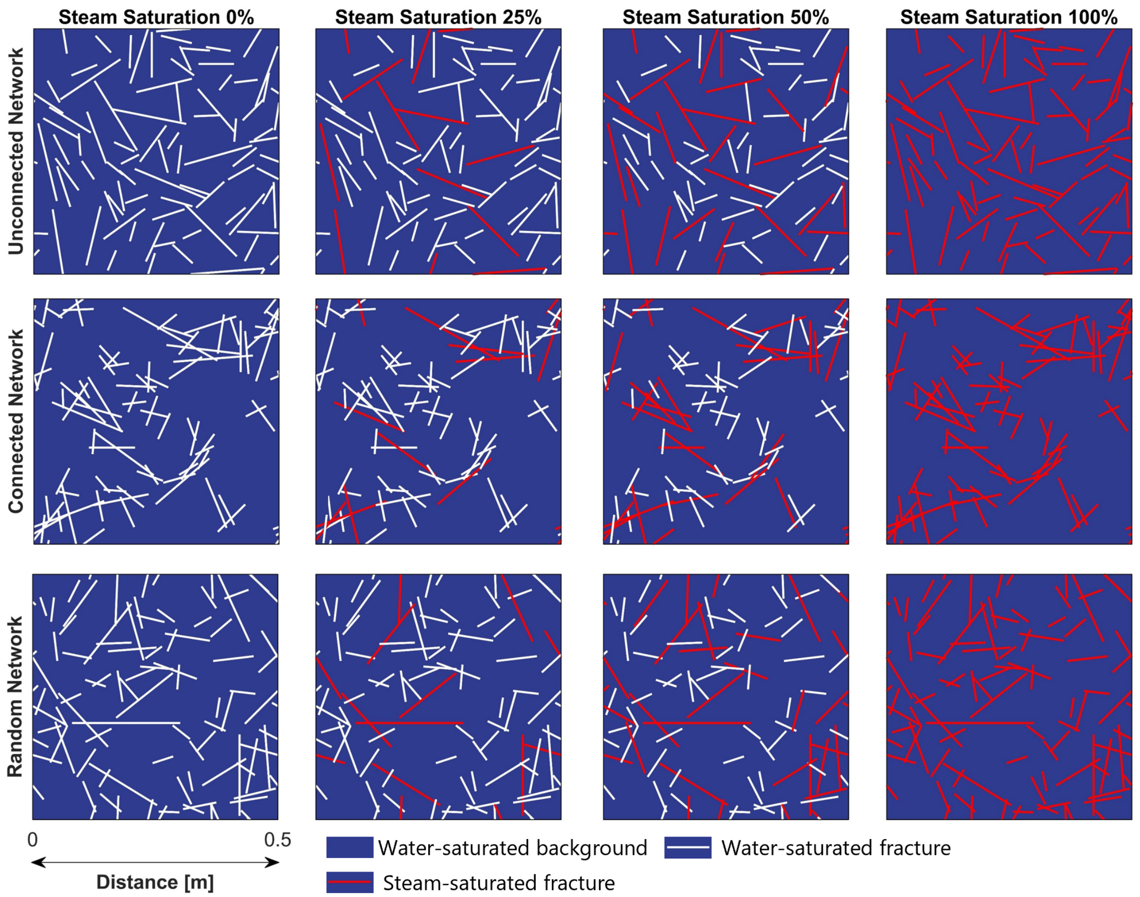

Figure 2: Examples of the fractured samples employed in the Monte Carlo procedure. Samples are 50 cm x 50 cm, the fracture area represents 1% of the total sample area, and the minimum and maximum fracture lengths are 4 and 25 cm, respectively. White-colored fractures denote brine-saturation while red-colored fractures denote saturation by steam. The top row represents totally unconnected fracture networks, the middle row totally connected fracture networks, and the bottom row randomly connected fracture networks. Steam saturation increases from left to right.

(Figure 1f). If the intersecting fractures contain fluids with differing compressibilities, such as liquid and gas, fracture-to-background FPD effects are diminished in comparison to fully water-saturated fractures (e.g., Kong et al., 2013; Solazzi et al., 2020). This is due to the fact that the lower compressibility of gas allows for a lower overall equilibrium pressure within the fractures, thus, reducing the pressure gradient between the fractures and the background and, hence, resulting in smaller fracture-to background FPD. The presence of varying fracture saturation also affects fracture-to-fracture FPD, but, in this case, the orientation of the fractures with regard to the incident P- or S-waves affects the outcome (Solazzi et al., 2020). Depending on whether the liquid or the gas are compressed by the seismic waves, FPD effects are either enhanced or diminished. If the liquid phase is preferentially compressed, the more compliant gas allows for a larger amount of liquid to flow into the connected gas-saturated fractures as compared to the scenario of both fractures being saturated with liquid. This increase in fluid flow translates into stronger FPD effects. Conversely, when the more compliant gaseous phase is preferentially compressed, the increase in pressure is less pronounced, which, in turn, does not favor FPD between connected fractures.

When looking at the associated frequency ranges, fracture-to-background FPD tends to occur at lower frequencies than fracture-to-fracture FPD, because the characteristic frequencies of these FPD manifestations are proportional to the permeability of the regions experiencing fluid flow. Given that the permeability of the embedding background is inherently much smaller than that of the fractures, fracture-to-background FPD occurs over a longer timescale and, thus, prevails at lower frequencies than fracture-to-fracture FPD. Above the frequency range, at which fracture-to-background FPD prevails, the sample behaves as if the fractures were hydraulically isolated from the background. The frequency range between the fracture-to-background and fracture-to-fracture FPD regimes is characterized by pressure equilibrium within connected fractures, which substantially reduces the stiffening effect of the fracture fluid compared to the high-frequency limit (Rubino et al., 2017). Correspondingly, this frequency range presents little to no velocity dispersion, and is hereafter denoted as the "non-dispersive plateau" (Figure 1e), in which the medium essentially behaves elastically. It is worth noting that, in the presence of two fluid phases, the frequency range, at which fracture-to-fracture FPD prevails, can be wider than in the case of single-phase saturation (Solazzi et al., 2020). For frequencies higher than those, at which fracture-to-fracture FPD prevails, the sample behaves as if fractures were hydraulically isolated from the background and from each other, as there is not enough time during a half wave cycle for pressure diffusion to occur. This is the so-called no-flow or high-frequency limit (Figure 1g), beyond which the medium essentially behaves elastically.

It is important to remark here that although there is neither attenuation nor velocity dispersion in the frequency range covered by the non-dispersive plateau, seismic velocities are inherently lower than those associated with the high-frequency elastic limit (Figure 1h). This means that, even though the body wave velocities in the non-dispersive plateau are representative of a non-dispersive, elastic medium, they can only be adequately modelled by accounting for the prevailing FPD effects.

RESULTS

Seismic response of partially saturated fractured granite

In order to obtain the mechanical response of a fractured granite, which is a typical environment hosting high-enthalpy geothermal reservoirs, we employ the physical properties listed in Table 1. The rock physical properties of granite correspond to those listed in Detournay and Cheng (1993). We model the fractures as very soft, porous and permeable inclusions whose grain level properties correspond to those of the embedding granitic background. Fractures have fixed properties regardless of their length, which were adapted from Rubino et al. (2017). The permeability of the fractures is 9 orders-of-magnitude higher than that of the background, and the resulting normal and shear compliances of the fractures are consistent with recent field measurements (e.g., Barbosa et al., 2019). We consider water as the main saturating fluid and steam as the secondary fluid. The properties of water and steam are a matter of study in several works, as the interactions between the two phases can be complex (e.g., Grab et al., 2017). For simplicity, we consider water and steam to be separated phases that do not interact with each other in terms of mixing or heat transfer during the passage of seismic waves. This first-order approximation results in the maximum difference between the module of the gaseous and liquid phases, which, in turn, implies that our results represent a best-case scenario with regard to

Rock	Granite Background	Fractures
Solid grain density (ρ^S)	2700 kg/m^3	2700 kg/m^3
Solid grain bulk modulus (K^S)	45 GPa	45 GPa
Dry frame shear modulus(μ^d)	19 GPa	0.02 GPa
Dry frame bulk modulus (K^d)	35 GPa	0.04 GPa
Permeability	1e-19 m^2	1e-10 m^2
Porosity (ϕ)	0.02	0.8
Fluid	**Brine**	**Steam**
Fluid viscosity (η)	6.6e$-$5 Pa.s	2.38e$-$5 Pa.s
Fluid bulk modulus (K^f)	0.191 GPa	0.0229 GPa
Fluid density (ρ^f)	574 kg/m^3	113 kg/m^3

Table 1: Properties of intact granitic background and embedded fractures. Granite properties were taken from Detournay and Cheng (1993). Fractures are represented as highly compliant, porous, and permeable inclusions, whose grain-level properties correspond to those of the embedding background (Rubino et al., 2017). Fluid properties correspond to a temperature of 350 degrees Celsius and a pressure of 167 bar for brine, and the same temperature and a pressure of 165 bar for steam. These properties are obtained from the XSTEAM matlab routine (Holmgren, 2006).

the sensitivity of seismic methods to the presence of steam. The properties of the fluids are obtained from the XSTEAM Matlab subroutine (Holmgren, 2006) following the standards of the International Association of the Properties of Water and Steam (IAPWS). In our model, we consider a fixed temperature of 350 °C and a pressure of approximately 167 bar for the liquid water phase. The latter corresponds to the saturation pressure of liquid water for that temperature. For the fractures containing steam, we consider a pore fluid pressure of 165 bar, which allows for the existence of such gaseous phase. We assume that such decrement of pressure does not affect any other properties of the fractured rock.

We employ the upscaling procedure described in the Methodology section on square samples with a side length of 50 cm, with rectangular fractures corresponding to a fracture density $Fd = 1\%$, as schematically illustrated in 2. We consider fractures with a stochastic distribution of fracture lengths with an $L_{max} = 25$ cm; $L_{min} = 4$ cm, and a fixed aperture of 0.4 mm. These values correspond to aspect ratios between 625 and 100, which are consistent with values observed in nature (e.g., Vermilye and Scholz, 1995). We define the fracture steam saturation S_s^f as

$$S_s^f = 100 * V_s^f / V_p^f [\%], \tag{11}$$

where V_p^f is the total pore volume of the fractures and V_s^f is the fracture pore volume saturated with steam. We compute velocities for S_s^f-values of 0, 10, 25, 50, 75 and 100%. For this, we generate 50 realizations for each of the three fracture connectivity degrees described earlier and for each fracture steam saturation modelled. As illustrated in Appendix B, we found that this number of realizations is sufficient

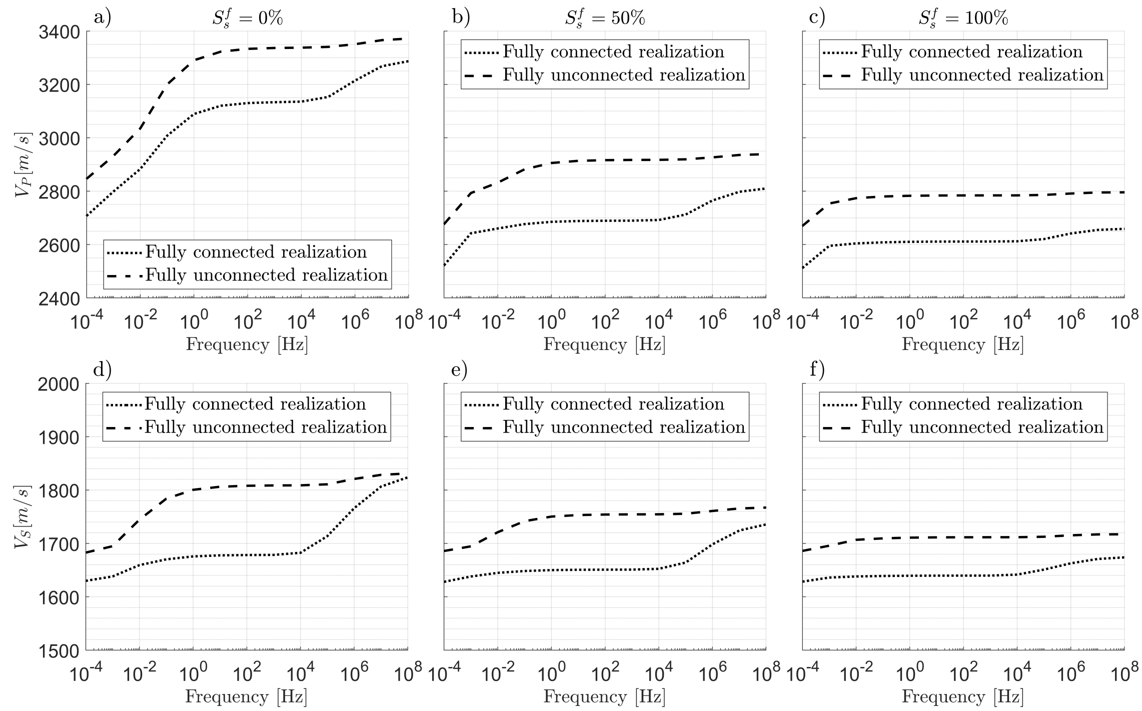

Figure 3: (a, b, c) P- and (d, e, f) S-wave velocities as functions of frequency for a single realization of connected (dotted lines) and unconnected (dashed lines) fracture networks. Steam saturation of the fractures S_s^f is (a, d) 0%, (b, e) 50% and (c, f) 100%.

for stabilizing the standard deviations of the velocity in the non-dispersive plateau, which is the convergence criterion of the employed Monte Carlo approach (Rubino et al., 2009). It is important to mention that, for representative effective velocities and an a upper frequency limit of 60 Hz, the ratio of wavelength to fracture length is at least 40 for P-waves and 25 for S-waves. This is consistent with the assumption of mesoscale fractures in our upscaling procedure. Figure 3 shows the P- and S-wave velocities as functions of frequency for single samples, that is, for individual fracture networks of the ensembles used to get averaged representative values for the non-dispersive plateau. Even though such realizations do not constitute representative samples, the results shown in Figure 3 allow to illustrate the effects of FPD on the body wave velocities of the samples. Velocity values are shown for the connected (dotted lines) and unconnected (dashed lines) cases as well as for different levels of steam saturation of the fractures. Two manifestations of velocity dispersion can be discerned, one around 10^{-2} Hz corresponding to fracture-to-background FPD and the other around 10^{6} Hz corresponding to fracture-to-fracture FPD. The non-dispersive plateau is located between these two distinct FPD manifestations, where increasing levels of fracture connectivity are associated with significantly lower P- and S-wave velocities. Please note that the non-dispersive plateau includes the typical frequencies of active and passive seismic exploration and monitoring methods (approximately 0.1 Hz to 60 Hz). In this frequency range, there is not enough time in a half wave cycle to allow for pressure diffusion between the fractures and background. This means that, in the case of isolated fractures, the fluid contained inside the fractures has a significant stiffening effect in response to compressional forces. For the case of connected fractures, however, there is enough time to allow pressure to equilibrate between connected fractures, thus, greatly diminishing the fluid stiffening effect and, correspondingly, lowering the velocities of the formation. These mechanisms explains the lower velocity values for connected fracture networks in comparison to unconnected fracture networks for seismic frequencies, regardless of the saturation state in the fractures.

Again, focusing on the frequencies comprised by the non-dispersive plateau, let us now analyze the effects that partial steam saturation of the fractures has on the body wave velocities of the formation. We observe different behaviors for P- and S-wave velocities and for different connectivities of the fracture network. For P-wave velocities the marked velocity drop associated with increasing S_s^f is particularly important, indicating that P-wave velocities are adequate to detect and monitor the initial appearance of steam (Figures 3a, 3b, and 3c). In the case of S-wave velocities, we observe that the velocity drops associated with different levels of steam saturation are much less pronounced than for P-waves (Figures 3d, 3e, and 3f). These are interesting results, as Solazzi et al. (2020) reports significant effects for both P- and S-waves in a context of partial saturation of fractures with brine and CO_2. Notably, the S-wave velocities drop due to changes in fluid content are comparable to possible changes in connectivity for a fully water-saturated fracture network. In the case of P-wave velocities, on the other hand, changes associated with fluid content are much larger than those associated with changes in connectivity for a fully water-saturated fracture network.

When looking at values in the high-frequency limit, we observe that the differences between connected and unconnected cases are much narrower than those corresponding to the non-dispersive plateau. These values correspond to a high-frequency elastic representation that does not consider hydraulic communication between connected fractures. In the following, we analyze the results obtained from the Monte-Carlo-type procedure described in the Methodology section for velocities corresponding to (i) the non-dispersive plateau and to (ii) the high-frequency limit of the medium.

Figure 4 shows the effective body wave velocities as functions of the steam saturation for different fracture connectivities and different frequency regimes, obtained by means of the Monte Carlo approach. The frequency regimes correspond to (i) the non-dispersive plateau (employing the velocity values for 10 Hz), in the following denominated as the *poroelastic approach*, and to (ii) the high-frequency elastic behavior of the formation, which we also refer to as *elastic*, as it corresponds to the response of an elastic background that contains elastic fractures (inclusions).

Figures 4a, 4b, and 4c show V_P as function of S_s^f for fully connected, randomly connected, and unconnected fracture networks, respectively, for both poroelastic (red lines) and elastic (blue lines) approaches. We observe that, in all cases, V_P decreases with increasing steam saturation in a similar way for the poroelastic and elastic models. The velocity values associated with these two cases, however, differ significantly when FPD within connected fractures is present. This is to be expected as these modelling approaches differ significantly when fracture connectivity is present, whereas in the unconnected case the responses are quite similar. We also observe that changes in V_P are more pronounced for values of S_s^f below 50%. For S-waves (Figures 4d, 4e, and 4f), we observe that, as in the case of V_P, while there are significant changes between the poroelastic and elastic responses randomly or fully connected networks, they are quite similar for the unconnected case. Moreover, we see that in the fully connected or randomly connected cases, the S-wave velocity turns out to be virtually insensitive to steam saturation when FPD effects are accounted for. This, in contrast with the P-wave velocity, indicates that FPD effects have a comparatively more sig-

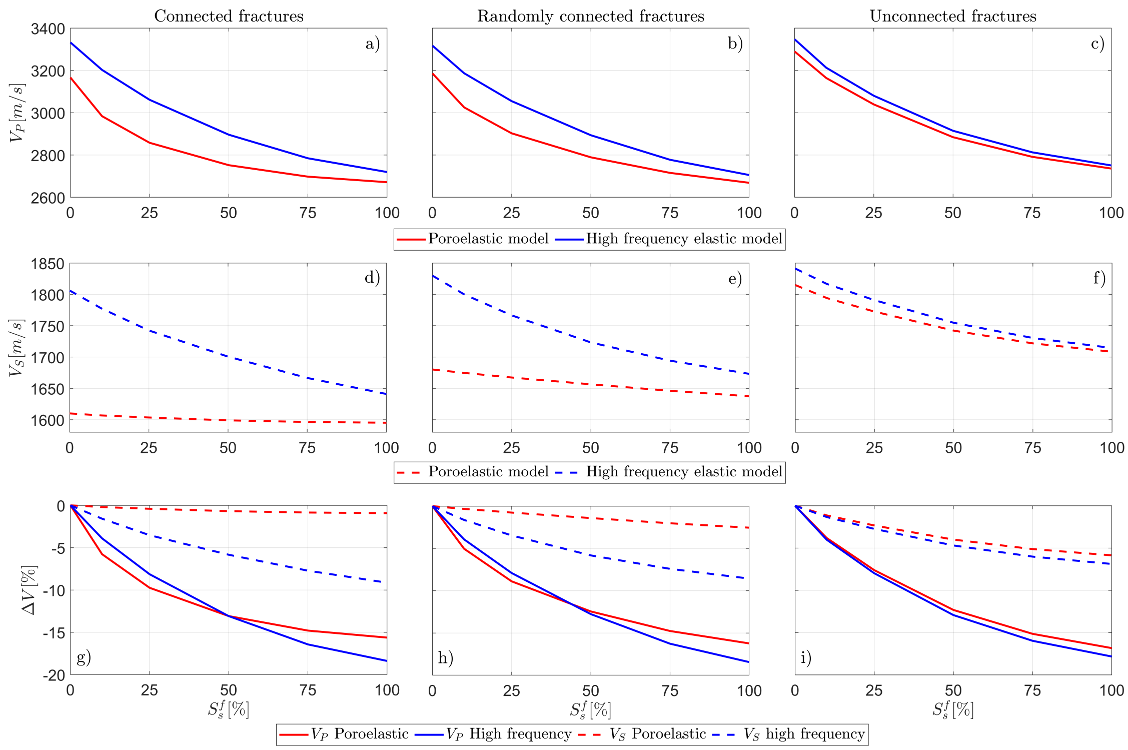

Figure 4: (a, b, c) P- and (d, e, f) S-wave velocities as functions of steam saturation S_s^f for different fracture connectivity scenarios. Blue lines correspond to the elastic high-frequency limit and red lines to seismic frequencies within the non-dispersive plateau. The relative velocity change for each connectivity level (g, h, i) is computed as $\Delta V = \frac{V_{P,S}(S_s^f) - V_{P,S}(S_s^f=0)}{V_{P,S}(S_s^f=0)}$, and is shown for V_P (continuous lines) and V_S (dashed lines).

nificant impact for S-waves. We remark that fully unconnected fracture networks for a fracture density such as the one we consider here are unlikely in nature, and that this end-member-type scenario is shown for comparison purposes.

As previously stated, velocity changes associated with S_s^f are shown in more detail in Figures 4g, 4h, and 4i, which depict the relative changes with respect to $S_s^f = 0$. We can observe that the resulting relative differences for the unconnected case are similar for the poroelastic and the elastic approaches. However, in the case of fully connected (Figure 4g) and randomly connected (Figure 4h) fracture networks, there are clear differences between these models. These differences are particularly significant when considering S-wave velocities, where the poroelastic approach presents practically no changes with respect to S_s^f (red dashed lines), while the elastic model shows much higher relative changes (blue dashed lines). This result shows that employing classic elastic approaches may lead to an overestimation of the sensitivity of S-wave velocities to changes in saturation in fractured media. It is worth noting that, while S-wave velocities appear to be insensitive to changes in saturation in fractured media for the fully connected and randomly connected cases, previous research shows that they are sensitive to changes in fracture density in a geothermal reservoir context (e.g., Quiroga et al., 2022).

Given that changes of both fracture density and steam saturation can result from pressure fluctuations in geothermal reservoirs, let us analyze the sensitivity of P- and S-wave velocities to both parameters. For this, we use data from Quiroga et al. (2022) where the sensitivity of P- and S-wave velocity to changes in fracture density was

Formation	Fd	V_P [m/s]	V_S [m/s]	ρ_b [kg/m^3]
	0.25%	4687	2428	2694
Fractured	0.35%	4609	2321	2692
Granite	0.50%	4510	2186	2690
	0.60%	4451	2088	2688
	0.75%	4330	1929	2687
	0.90%	4270	1825	2683

Table 2: Mechanical properties of fractured granite with variable fracture densities. These characteristics correspond to randomly connected fractured granite saturated with brine ($K_f = 2250GPa, \eta = 1e^{-3}Pa.s$) for different Fd values. These values correspond to frequencies in the non-dispersive plateau. Taken from Quiroga et al. (2022).

analyzed. The upscaling procedure and the properties of the embedding background and the fractures are identical to the ones of this work. The key difference is that in Quiroga et al. (2022) both fractures and background are saturated with brine (K_f = 2250 GPa, η = $1e^{-3}$ Pa.s). The effective velocities are listed in Table 2 and correspond to randomly connected fracture networks with fracture density Fd percentages of 0.25, 0.35, 0.50, 0.60, 0.75, and 0.90.

In order to compare the effects of steam variation considered here and the effects of fracture density in brine-saturated media explored by Quiroga et al. (2022), the plotted P-velocity values of both studies are scaled by their respective maximum val-

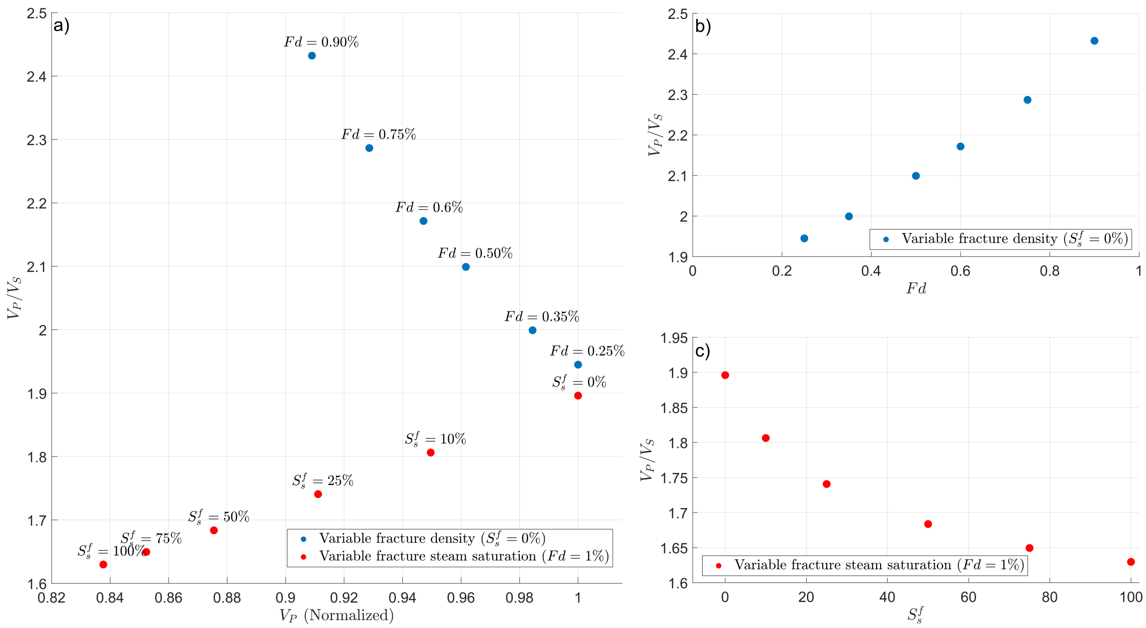

Figure 5: (a) Crossplot of V_P/V_S against V_P. Orange dots correspond to randomly connected fracture networks with a fixed fracture density Fd of 1% and varying S_s^f, from 0 to 100%. Blue dots were taken from Quiroga et al. (2022) and correspond to fracture networks with identical fracture properties, varying fracture density from 0.25% to 0.9% and water (K_f = 2250 GPa, $\eta = 1e^{-3}$ Pa.s) as the saturating fluid. V_P values are normalized with respect to the respective maximum values for ease of comparison. V_P-values for variable fracture density are divided by the value of V_P for $Fd = 0.25\%$ and the V_P-values for variable fracture steam saturation by the value of V_P for $S_s^f = 0\%$. (b) V_P/V_S ratio as a function of Fd for fracture networks with full water saturation. (c) V_P/V_S ratio as a function of S_s^f for fracture networks with fracture density $F_d = 1\%$.

ues in Figure 5a. The highest P-wave velocity values occur for $S_s^f = 0\%$ in our current study and for a fracture density $Fd = 0.25\%$ for the study performed in Quiroga et al. (2022). Both increments in S_s^f and Fd are associated with similar relative decrements in P-wave velocity, therefore, it would not be possible to distinguish steam variations from fracture density changes using this parameter alone. However, the behavior of S-wave velocities allows us to distinguish between these characteristics. As shown in Figure 5b, increments of fracture density are associated with increases in the V_P/V_S ratio. Conversely, increasing presence of steam in the fractures is associated with decrements in the corresponding V_P/V_S ratio (Figure 5c). This result shows that there is a possibility for certain techniques, or combinations thereof, to identify the causes behind commonly observed velocity drops in geothermal monitoring surveys (e.g., Taira et al., 2018; Obermann et al., 2015).

Impact of partial saturation on seismic monitoring techniques

Let us now explore the impact of the presence of steam on seismic monitoring methods. For this, we consider the canonical model of a high-enthalpy geothermal reservoir as depicted in Figure 6. We assume that the reservoir has a temperature of 350°C. In order to be close to the saturation pressure of liquid water, which, for this temperature, is approximately $1.67{\times}10^7$ Pa or 167 bar. Considering a normal lithostatic pressure gradient (e.g., Tiab and Donaldson, 2015), this corresponds to a depth of approximately 700 m.

The physical properties of the geological model employed are described in Table

Formation	Lithology	Depth	S_s^f	V_P [m/s]	V_S [m/s]	ρ_b [kg/m^3]
Overburden	Sandstone	0-600 m	-	3000	1600	2500
Upper reservoir	Partially saturated fractured granite	600-800 m	0%	3186	1680	2684
			10%	3025	1675	2683
			25%	2902	1667	2683
			50%	2789	1656	2682
			75%	2715	1646	2681
			100%	2668	1637	2681
Lower reservoir	Fractured granite	800-1000 m	0%	3186	1680	2684
Basement	Intact granite	1000-∞ m	-	4810	2620	2700

Table 3: Properties of the geological model

3. This model consists of a surficial layer of homogeneous sandstone to 600 m depth, below which the reservoir formation is located. This layer consists of 400 m of fractured granite, which we consider to be divided in two different sections. The upper section of the reservoir is located at depths between 600 m and 800 m, and can have either steam or water in its fractures. The lower section of the reservoir is located between 800 m and 1000 m depth, and it is saturated exclusively with water, as, at these depths the higher lithostatic pressure does not allow for the occurrence of steam. Below the reservoir formation, there is a semi-infinite layer of intact granite, with the same petrophysical properties as the background reservoir rock (Table 1). The sandstone layer and the intact granite basement are considered homogeneous and elastic, and, hence, seismic waves traversing them are not attenuated or dispersed. Conversely, the seismic velocities for the upper and lower reservoir are those obtained from the upscaling procedure (Figure 4). We consider for the upper reservoir different values of S_s^f, while the lower reservoir is fully saturated with water. We employ the velocity values corresponding to randomly connected fracture networks, as it is the case that can be considered as more realistic compared to the end-member type scenarios of completely unconnected or completely connected fracture networks explored in the previous section. In the following, we utilize this model to simulate results related to Rayleigh wave monitoring and reflection seismic surveys.

Rayleigh wave dispersion modelling

To compute Rayleigh wave velocity dispersion, we employ the so-called fast delta matrix algorithm (Buchen and Ben-Hador, 1996). This algorithm considers homogeneous horizontal layers with no velocity dispersion. Although we are employing a poroelastic upscaling procedure that accounts for velocity dispersion due to FPD, for the frequencies of interest for this analysis (∼0.1 Hz to ∼3 Hz) fall into the non-dispersive plateau and the corresponding velocities, thus, present negligible velocity dispersion (Figure 3). As absolute differences between Rayleigh wave dispersion curves might be difficult to discern, we compute relative velocity differences as $\Delta V_{p,g}(S_s^f) = max_{freq}(\frac{V_{p,g}(S_s^f)-V_{p,g}(0)}{V_{p,g}(0)})$, that is, $\Delta V_{p,g}$ is the relative velocity difference for the frequency where it attains its maximum value, $V_{p,g}(S_s^f)$ is the frequency-dependent Rayleigh wave velocity for a given S_s^f and $V_{p,g}(0)$ is the Rayleigh wave velocity for $S_s^f = 0$. The subindexes p, g denote phase and group velocities, respectively. To model the sensitivity of Rayleigh wave based methods to different fracture steam saturation, we consider different values of S_s^f in the upper part of the reservoir. The results of the Rayleigh wave phase and group velocity, as well as the associated relative velocity differences for different S_s^f values, are shown in Figure 7.

Figures 7a and 7b show the Rayleigh wave phase and group velocity dispersion considering the poroelastic and elastic approaches, respectively. For both phase and group velocities and for both approaches, we observe higher velocities for low frequencies, due to the fact that Rayleigh waves penetrate deeper due to the correspondingly longer wavelengths. This corresponds to the stiffer intact granitic basement in our

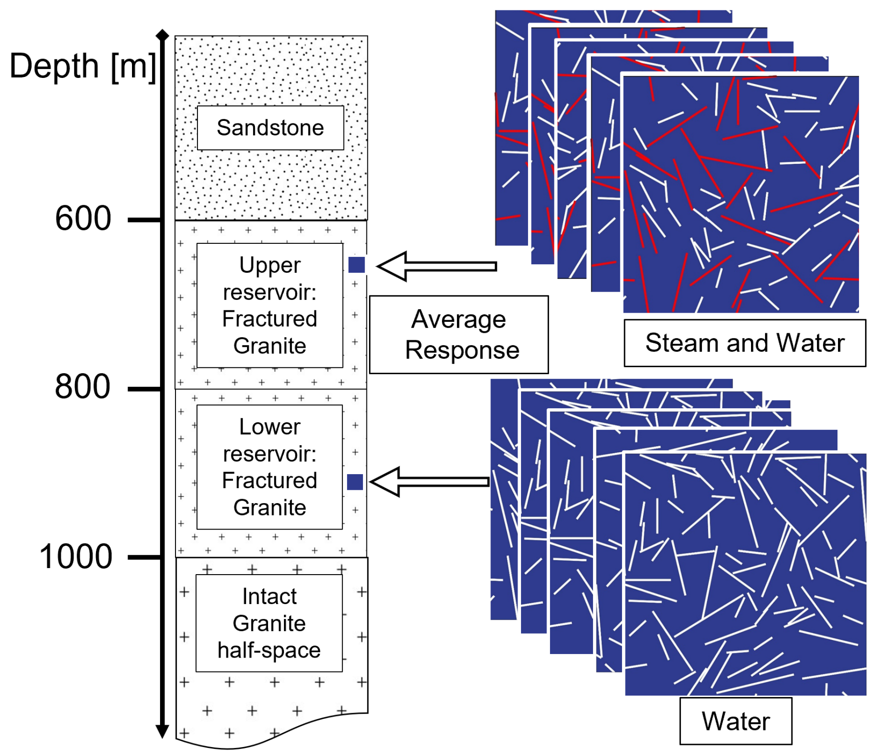

Figure 6: Schematic representation of the geothermal reservoir model employed in the analysis. The sandstone and intact granitic layers are considered to be homogeneous, while the granitic reservoir is characterized as a fractured formation with the fractures being saturated with either water and steam (upper part of the reservoir) and only water (lower part of the reservoir).

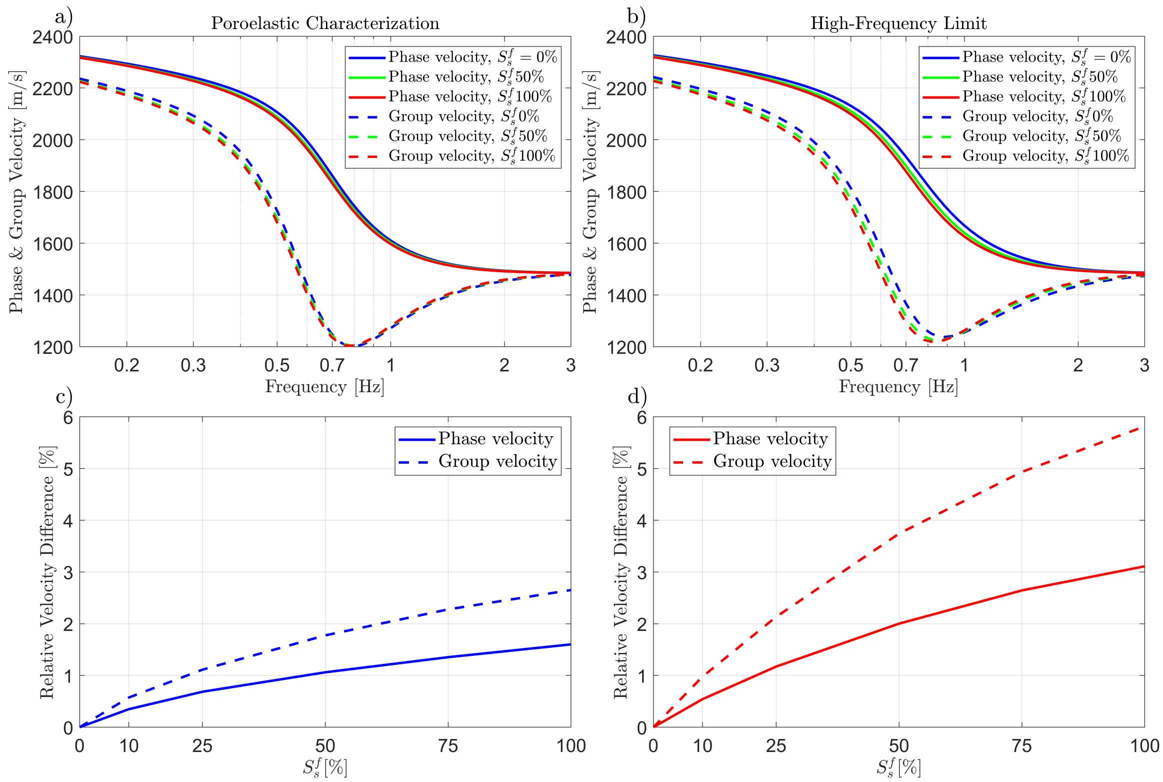

Figure 7: (a, b) Phase and group velocity dispersion of Rayleigh waves for the model described in Table 3 for different levels of steam saturation in the upper part of the reservoir, considering (a) a poroelastic and (b) an elastic approach. Relative velocity difference ($\Delta V_p, g(S_s^f)$) for phase (solid lines) and group velocities (dashed lines) for (c) poroelastic and (d) elastic approaches. Relative velocity differences are computed as the maximum difference between the dispersion at a certain steam saturation and the dispersion corresponding to a steam saturation of 0% divided by the value of the latter.

model. In addition, the velocities decrease as the frequency increases, and we can observe that the frequencies where variations of S_s^f have an impact on the Rayleigh wave measurements are comprised between 0.2 Hz and 1.5 Hz. It is also worth noting that there is a discrepancy between the modelled impact of steam saturation using a poroelastic approach and an elastic approach. This discrepancy may lead to an overestimation of the ability of Rayleigh-wave-based techniques to detect the presence of steam in geothermal reservoirs. Figures 7c and 7d show the relative difference between varying degrees of steam saturation in the upper reservoir and the case of an upper reservoir without the presence of any steam. As the impact of partial saturation on S-waves is limited when FPD are taken into account, we observe that, in this case, the relative velocity changes in Rayleigh wave velocity dispersion amount to a maximum of $\sim$3% for the case of Rayleigh group velocities and less than 2% when steam saturation goes from 0% to 100%. We observe that the relative changes for the elastic approach are almost double those of the models considering FPD effects.

It is interesting to compare the corresponding impact of varying S_s^f or fracture density Fd. As shown in Figure 5, changes of Fd from 0.25 % to 0.90% produce relative variations of P-wave velocity similar to those produced by changes in S_s^f for the properties considered in this work. To explore the sensitivity of Rayleigh wave velocity dispersion to changes in Fd we consider the reservoir's properties listed in Table 2. We consider the extreme case of a lower reservoir composed of brine-saturated granite with a Fd of 0.25% and fully brine-saturated upper reservoir, with varying Fd. Based on this model, the maximal variation of Rayleigh wave velocities occurs when the upper reservoir changes its density from 0.25% to 0.90%, in which case the relative change in velocities is $\Delta V_{p,g}(0.90\%) = max_{freq}(\frac{V_{p,g}(0.90\%)-V_{p,g}(0.25\%)}{V_{p,g}(0.25\%)})$. In this case $V_{p,g}(0.90\%)$ and $V_{p,g}(0.25\%)$ correspond to the Rayleigh wave phase and group velocities for the corresponding values of Fd in the upper reservoir. $\Delta V_{p,g}(0.90\%)$ amounts to 17% and 7% for Rayleigh wave group and phase velocities, respectively. These results, compared to the values of 3% and 2% corresponding to the most extreme changes in steam saturation, show that Rayleigh wave monitoring is considerably more sensitive to changes in mechanical properties due to fracture density increments than to changes in the fluid content of the fractures, as the former have a more pronounced relative impact on the S-wave velocity.

AVA modelling

Given that, as previously shown, the impact of partial saturation is most important with regard to the P-wave velocity, reflection seismic methods are expected to be more sensitive than surface-wave-based techniques to variations in the fluid content of a fractured reservoir. To assess this hypothesis, we again employ the geological model defined by Table 3 to compute its amplitude-versus-angle (AVA) seismic response. The AVA response of an interface is affected by changes in P- and S-wave velocities, and, considering the body wave velocity results previously shown, we may expect to obtain information about the fluid content of the formation. For this, we consider the target of the AVA inversion to be the intra-reservoir interface located at 800 m between the upper part of the reservoir with the presence of steam in its fractures and the lower part of the reservoir that is completely saturated by water (Table 3). This will provide insights on whether or not reflection seismics can, in principle, identify the lower limit of steam caps in geothermal reservoirs.

Considering that for typical surface-based seismic reflection analyses, the thicknesses of the layers involved in the considered geological model are larger than the predominant seismic wavelengths, the AVA response at the target interface can be modelled using Zoeppritz's equations (e.g., Dvorkin et al., 2014). These equations exactly model the reflection coefficients as a function of incidence angle at an interface between two homogeneous elastic solids. As the frequencies of interest of reflection seismics (approximately from 20 to 60 Hz) fall into the non-dispersive plateau for our study, the lower and upper parts of the reservoir behave as elastic solids, and Zoeppritz's equations can indeed be employed. We employ the implementation of Zoeppritz equations by Hall (2015) to compute the P-wave reflection coefficient of the intra-reservoir interface for different values of S_s^f for the upper part while the lower part is fully saturated with water. Figure 8a shows the P-wave reflection coefficient of the intra-reservoir interface as a function of incidence angle. Different colors correspond to different percentages of fractures saturated by steam in the upper part of the reservoir. Solid lines correspond to the poroelastic approach for modelling the response of the reservoir and dashed lines to the elastic approach. It is worth noting that the AVA response of the formation in both cases does not present significant variations for low angles.

In practice, AVA analysis consists of extracting the properties of the subsurface from the inversion of observed reflection coefficients. To do so, it is common practice to employ a linearized approximation of Zoeppritz' equations (e.g., Mavko et al., 1998) to retrieve impedances and velocities from reflection coefficients. We employ two classic approximations due to their widespread presence in the literature and considering that the information they can infer from seismic data may be different due to the different assumptions employed by the respective authors (e.g., Thomas et al., 2016). One of the approximations we employ is that of Fatti et al. (1994), which in its two-term version approximates the P-wave reflectivity R_{PP} as function of incidence angle θ as

$$R_{PP}(\theta) = (1 + \tan^2\theta)\frac{\Delta I_P}{2I_P} - 8(\frac{V_S}{V_P})^2 \sin^2\theta \frac{\Delta I_S}{2I_S}, \tag{12}$$

where $\Delta I_{P,S}$ denotes the difference in P- or S-wave impedance across the interface and $I_{P,S}$ correspond to the average of the P- and S-impedances of both sides of the interface. Although the term $(\frac{V_S}{V_P})^2$ depends on the values to retrieve, we consider the usual approach of approximating it as $1/2$ for the inversion process. The other approximation we consider is based on that of Shuey (1985) and given by (e.g., Avseth et al., 2010)

$$R_{PP}(\theta) = A + G\sin^2\theta, \tag{13}$$

where A is known as the intercept and corresponds to the P-reflectivity for a normal incidence and G as the gradient and depends on the physical properties of the medium. In the following, we refer to Equations (12) and (13) simply as Fatti's and Shuey's approximations, respectively. We follow a least squares inversion procedure (e.g., Quiroga et al., 2018) to obtain the corresponding AVA coefficients from synthetic

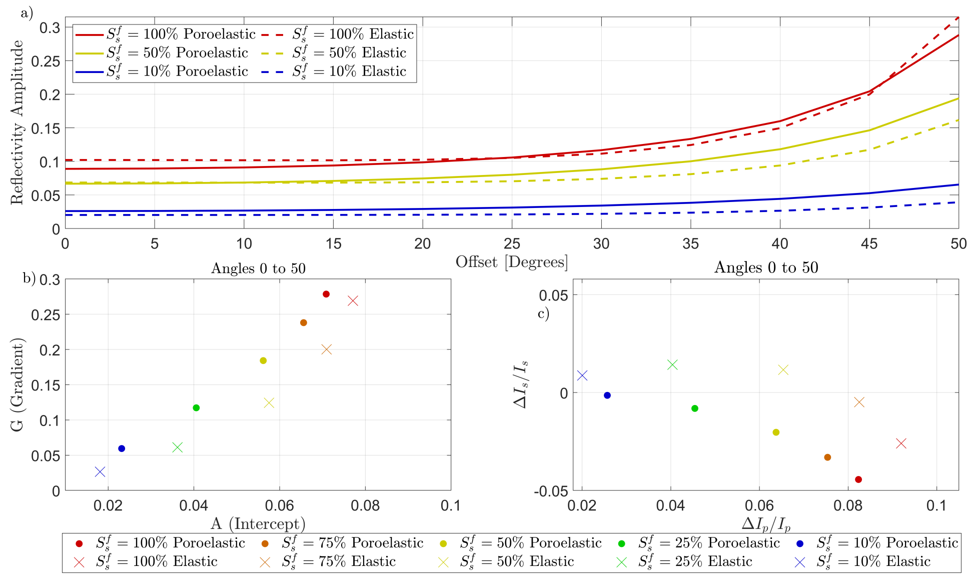

Figure 8: P-wave reflection coefficient and AVA coefficients for the interface between the partially steam-saturated upper part of the reservoir and the water-saturated lower part of the reservoir. (a) Reflectivity as a function of angle and S_s^f (100% red, 50% yellow, and 10% blue) for poroelastic (continuous lines) and elastic approaches (dashed lines). Results for the inversion using (b) Shuey's and (c) Fatti's approximations for incidence angles between 0° and 50°. Inversion results are shown for the poroelastic (dots) and for elastic (crosses) approaches.

reflectivity curves obtained using Zoeppritz's equations to explore their sensitivity to the steam saturation levels. For simplicity, we do not consider added noise in these simulations.

Figure 8b shows the results of inverting for AVA intercept A and gradient G (Equation 13), while Figure 8c shows those for the inversion of Fatti's coefficients $\Delta I_p/I_p$ and $\Delta I_s/I_s$ (Equation 12). For these inversion results, dots represent values obtained from the poroelastic representation and crosses those corresponding to the elastic response. We observe that there is a correlation of increases of steam saturation with increase of the coefficients A and G. We observe that both coefficients tend to increase as the degree of steam saturation increases (Figure 8b). However, while the behavior of the inversion corresponding to the poroelastic approach and that corresponding to the elastic approach are similar, there is a significant difference in the values of the coefficients, specially for lower values of steam saturation. This shows the importance of taking into account FPD effects for the detection and monitoring of steam. For the inversion based on Fatti's equation (Figure 8c) we observe that there is also sensitivity to steam saturation for both coefficients. In this case, however, we can see that the behavior of the poroelastic modelling differs significantly with regard to that of the elastic approach, as the results corresponding to the latter present positive values of $\Delta I_s/I_s$ for fracture steam saturation below 75% which are negative for the poroelastic approach. This is a very important distinction as it may lead to erroneous interpretations of reflection seismic data. These results indicate, in principle, that AVA analysis is appropriate for detecting the base of the steam cap in fractured geothermal reservoirs. Comparisons of the poroelastic and elastic approaches in Figures 8b and 8c show that there are significant differences between the AVA coefficients which, thus, points to the importance of FPD effects on such coefficients.

Considering the results for body wave velocities shown in Figure 5, it is also interesting to determine whether AVA inversion is useful to distinguish between variations

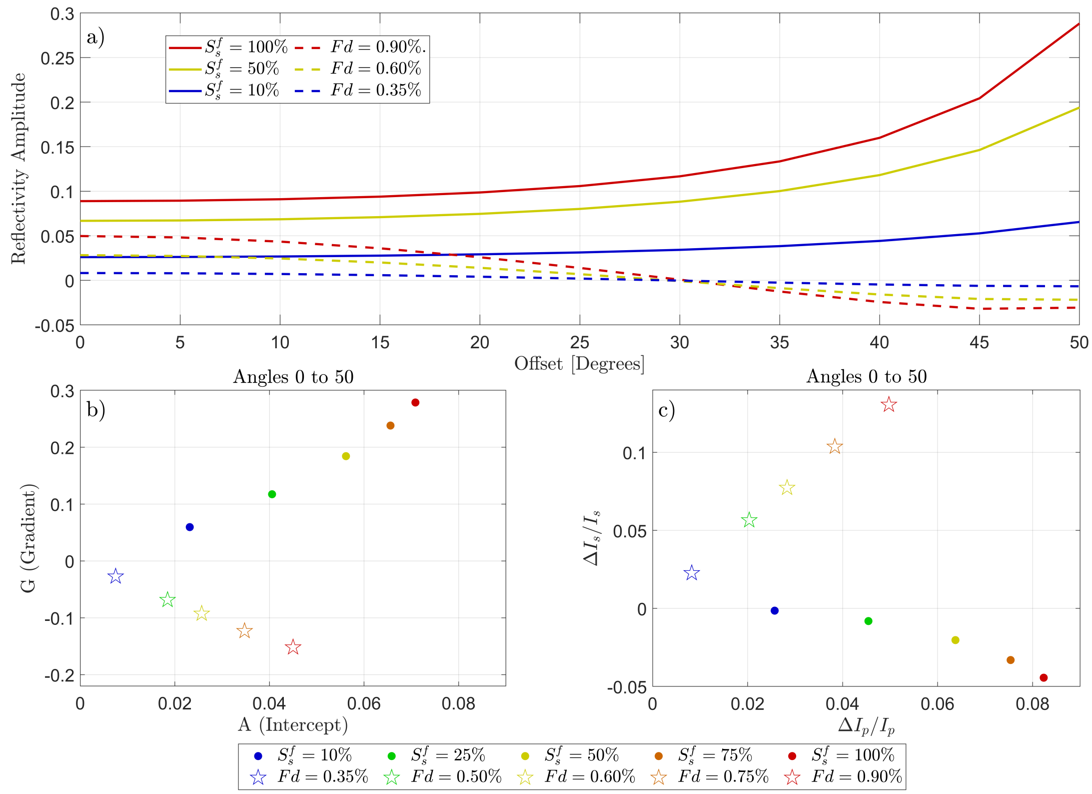

Figure 9: P-wave reflection coefficient as a function of incidence angle for the interfaces between: a partially steam-saturated upper part of the reservoir and a fully water-saturated lower part of the reservoir (solid lines); a fully water-saturated upper part of the reservoir with varying fracture density Fd over a fully water-saturated lower part of the reservoir with a Fd=0.25% (dashed lines). Results for the inversion using (b) Shuey's and (c) Fatti's approximations for incidence angles between 0 and 50°. Inversion results are shown for both variable S_s^f (dots) and the variable Fd scenarios (stars).

in steam saturation and fracture density. Employing the values for granitic rock with variable fracture density (Table 2) in the geological model of Table 3, we compare the results corresponding to changes in the steam saturation of the fractures and changes in fracture density. For variable fracture density AVA analysis, we consider the lower part of the reservoir to be composed of fractured granite with a fracture density of 0.25%, and the upper reservoir to have variable fracture density ranging from 0.35% to 0.90%. Figure 9 shows the reflectivity and the AVA inversion results for both cases for velocities corresponding to the non-dispersive plateau. In Figure 9a, we see the P-wave reflectivity for different values of saturation (solid lines) and different values of fracture density (dashed lines). We observe that the reflectivities at 0° incidence show some discrepancies, which become more significant with increasing incidence angle. This translates into a good separation in the crossplots of A vs G for Shuey's approximation (Figure 9b) and of $\Delta I_P/I_P$ vs $\Delta I_S/I_S$ for Fatti's approximation (Figure 9c). These results indicate that AVA crossplot analysis could be suitable for distinguishing between increases in fracture density and changes in fluid saturation.

DISCUSSION

In this work, we employed a numerical upscaling procedure in order to obtain effective seismic body wave velocities of granitic rocks containing mesoscopic fractures saturated with water or steam. In this context, it is important to note that the mesoscopic assumption allows us to study FPD effects by means of a numerical upscaling approach based on concepts of effective medium theory. However, the hyperbolic characteristics of fracture length distributions in nature implies that some fracture lengths will clearly exceed the considered mesoscale range. It is, in principle, possible to include mesoscopic fractures along with larger scale fractures whose length is comparable to the prevailing wavelengths in the seismic analysis and, thus, to account for both FPD and scattering effects. For this, one could perform wave propagation experiments using the effective properties derived in this work as those of the background while the larger-scale fractures would be represented by means of discrete fracture network (DFN) approaches (e.g., Lei and Sornette, 2021). An inherent limitation of this approach would be, however, that hydromechanical interaction between the mesoscopic and larger-scale fractures can not be considered.

As previously mentioned, when modelling partially saturated fracture networks, we consider fractures whose lengths obey a realistic power law distribution. However, we also apply some simplifications, both with regard to the mechanical and geometrical properties of the fractures as well in the way we saturate fractures. While we consider varying fracture lengths, we do not consider changes in the fractures' mechanical properties. This is an interesting and important topic for future research. We also consider fractures that have a rectangular shape and constant apertures, while in nature fractures present a wide range of complex geometries. Shape variations are expected to affect the mechanical properties of the fractures, for example, in the the presence of curved fracture surfaces, FPD manifestations may arise even when the fractures are isolated (Lissa et al., 2021). This is a vast field of research in its own and, hence, clearly exceeds the scope of this work, which focuses on first-order effects of partial steam saturation. Regarding our saturation approach, our main assumptions are that the background remains saturated with water at all times and that fractures are saturated completely with either steam or with water. Regarding the former, the embedding background rock is much more stiff than the fractures, and also considering that for seismic frequencies the background behaves as hydraulically isolated from the fractures, the potential presence of steam in the background would have a negligible effect in terms of the mechanical response of the medium. For the latter, if fractures were simultaneously saturated with both steam and water, this would, provided these fluids behave as immiscible, result in additional internal FPD effects within fractures (e.g., Solazzi et al., 2021). Recall that the distribution of fluids within individual fractures is governed by (i) the fracture properties, such as local variations in aperture (e.g., Hu et al., 2019) and (ii) the flow history (e.g., Chen et al., 2017). These effects are likely to be of subordinate importance in the given context. It is also important to note that, if fractures are simultaneously saturated by both water and steam, the assumption that these phases behave as immiscible may not be adequate, as thermodynamic fluid interactions could become important. In such a scenario, a model considering effective fluid properties might indeed be preferable (Grab et al., 2017).

When computing AVA reflectivities, we assume a sharp separation between the upper part of the reservoir, which is partially saturated with steam, and the lower part of the reservoir, which is fully saturated with water. In reality, the transition from full steam to full water saturation is likely to be progressive, which would compromise the sensitivity of AVA methods to detect the lower limit of the steam cap. Furthermore, while AVA inversion shows promise, there are situations for which it is not possible to determine the second term of the governing equations in an inversion, for example, when for logistical reasons, the offset range of seismic surveys is limited. In such situations, reflectivity measurements are still able to detect changes in the properties of the reservoir due to presence of steam, but it is not possible to differentiate the effects of increasing steam saturation to those related to increases of the density or connectivity of the fractures. Finally, as shown in the Results section, Rayleigh-wave-based methods are less sensitive to changes in the fluid content of the rock, but they are quite sensitive to changes in fracture density (Quiroga et al., 2022). It is, therefore, conceivable to employ Rayleigh wave inversion to complement P-wave impedance measurements, as both techniques are sensitive to changes in fracture density, while they respond very differently to changes in the fluid content of the reservoir.

CONCLUSIONS

In this work, we have analyzed the seismic response of a fractured granite formation with varying levels of steam saturation and different levels of fracture connectivity. We employed a poroelastic upscaling approach in a Monte Carlo fashion in order to obtain effective body wave velocities. The analysis of the effective body wave velocities of realistic samples reveal that partial steam saturation significantly affects the P-wave velocity while it does not have a significant impact on the S-wave velocity. These particularities are due to FPD effects and are not adequately modelled by an elastic approach. A comparison with previous works that investigate changes in fracture density and connectivity as driving causes for velocity drops observed during seismic monitoring of geothermal scenarios indicates that the effects of increasing steam saturation and fracture density can be differentiated through an analysis of the V_P/V_S ratio. To further develop this analysis, we incorporate these velocities in a geological model compatible with the presence of hot water and steam to assess the sensitivity of different characterization and monitoring techniques. We find that: (i) Rayleigh-wave-based techniques are much less sensitive to changes in fluid saturation compared to changes in fracture density, and that employing a purely elastic characterization may lead to an overestimation of the sensitivity of this method to such changes; (ii) AVA attributes are robust in characterizing discontinuities in fluid content but correct modelling of effects of FPD on the seismic velocities is required in order to improve the interpretation of the data, especially when the range of incidence angles is limited; and (iii) in zones where AVA characterization is not possible, P-wave velocity or P-impedance estimates could be potentially combined with Rayleigh wave monitoring in order discriminate between changes in steam saturation and fracture density.

ACKNOWLEDGMENTS

This work is supported by grant number 200020-178946 from the Swiss National Science Foundation. J. G. R. gratefully acknowledges the financial support received from

CONICET (grant PIP 11220210100346CO). Marco Favino gratefully acknowledges the financial support of the Swiss National Science Foundation (grant PZ00P2_180112). We wish to thank Junxin Guo and two anonymous reviewers for lucid comments and constructive suggestions, which allowed us to significantly improve the quality of this work.

APPENDIX A

POROELASTIC CHARACTERIZATION WORKFLOW

In the following, we summarize the steps required for the evaluation of effective seismic body wave velocity and attenuation characteristics of a formation. This approach is based on the theory of poroelasticity of Biot (1956a,b) and takes into account FPD effects. The underlying assumptions are that the heterogeneities in the probed formation are in the mesoscale range, that is, much larger than the pore scale but much smaller than the prevailing seismic wavelengths, and that the frequencies analyzed are sufficiently low to be able to ignore Biot's intrinsic attenuation effects. For upper crustal rocks with fractures below a meter in length and typical seismic frequencies (<60 Hz), these assumptions are safely met.

The workflow is then the following:

1. Obtain the poroelastic material properties of the rocks and fluids to be modelled. For the purpose of this study, the required properties and their sources are listed in Table 1.

2. Determine the statistical properties of the fractured formation, such as fracture

density, minimum and maximum fracture length, fracture aperture distribution, degree of fracture interconnectivity. Generate fractured rock samples with the desired statistical characteristics. For this study, we employ a fixed fracture density, a power law distribution of lengths, described by Equation 10 (Hunziker et al., 2018), and an iterative fracture placement procedure to obtain different degrees of fracture interconnectivity. We also model different degrees of steam saturation of the fractures of the samples by completely saturating individual fractures until the desired steam saturation has been reached.

3. Apply the upscaling procedure described in the Methodology section and schematically outlined in Figure 1 to the rock samples to obtain the volumetric average of stress and strain (Rubino et al., 2016; Favino et al., 2020).

4. Follow the procedures described in Rubino et al. (2016) to obtain the frequency-dependent effective stiffness matrix coefficients and, thus, obtain the P- and S-wave velocities and attenuation.

5. In order to obtain the effective seismic velocities, average the results associated with samples sharing the same statistical characteristics. In our study, we average samples that share the same fracture density, degree of interconnectivity and steam saturation percentage. The averaged values can be considered as representative of the formation of interest once the standard deviation of the resulting properties as a function of the number of samples averaged stabilizes (Rubino et al., 2009).

APPENDIX B

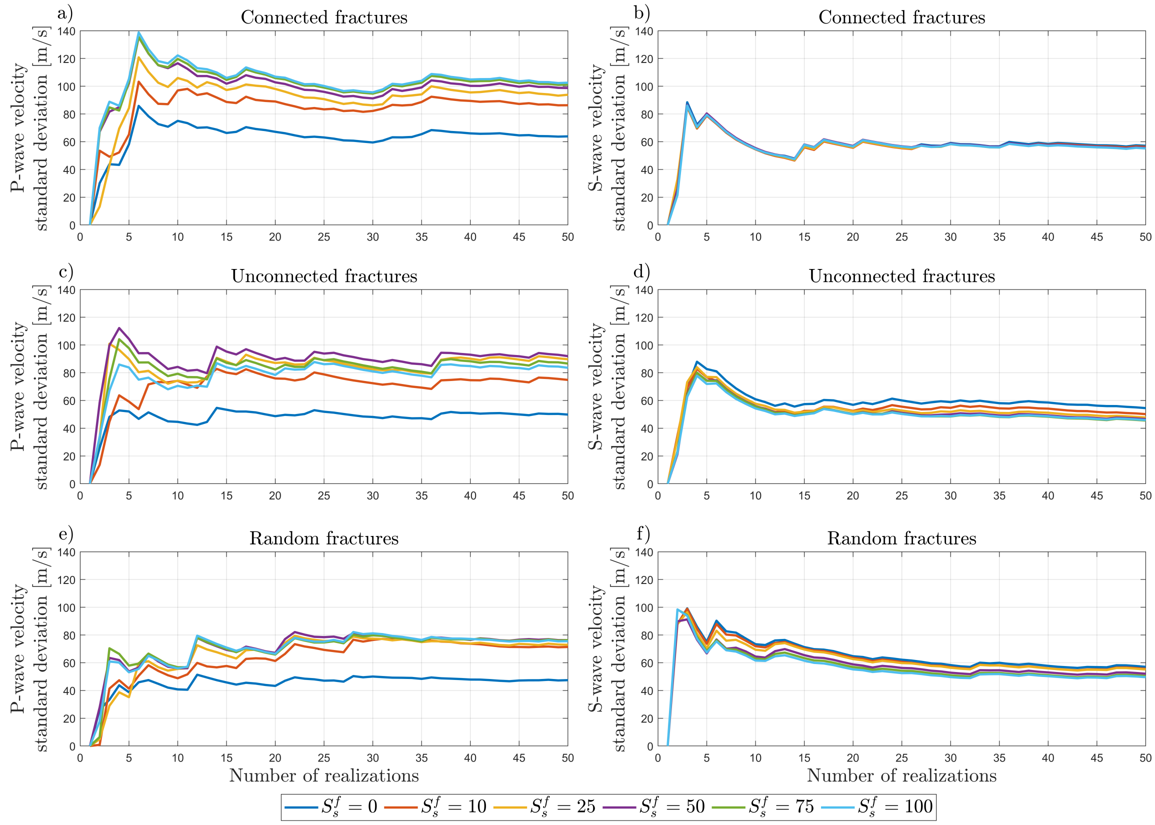

Figure B-1

STANDARD DEVIATION OF THE EFFECTIVE VELOCITIES

Figure B-1 depicts the evolution of the standard deviation of the effective velocities as a function of the number of stochastic realizations averaged for fully unconnected, fully connected, and randomly connected fracture network realizations. The stabilization of this value is indicative of the convergence of the Monte Carlo procedure (Rubino et al., 2009). In view of these results, we consider an average of 50 realizations as representative of the effective velocities of the considered fractured media.

REFERENCES

Avseth, P., T. Mukerji, and G. Mavko, 2010, Quantitative seismic interpretation: Applying rock physics tools to reduce interpretation risk: Cambridge university press.

Barbier, E., 2002, Geothermal energy technology and current status: an overview: Renewable and Sustainable Energy Reviews, **6**, 3–65.

Barbosa, N. D., E. Caspari, J. G. Rubino, A. Greenwood, L. Baron, and K. Holliger, 2019, Estimation of fracture compliance from attenuation and velocity analysis of full-waveform sonic log data: Journal of Geophysical Research: Solid Earth, **124**, 2738–2761.

Biot, M. A., 1941, General theory of three-dimensional consolidation: Journal of Applied Physics, **12**, 155–164.

———, 1956a, Theory of propagation of elastic waves in a fluid-saturated porous solid. I. Low-frequency range: The Journal of the Acoustical Society of America, **28**, 168–178.

———, 1956b, Theory of propagation of elastic waves in a fluid-saturated porous solid. II. Higher frequency range: The Journal of the Acoustical Society of America, **28**, 179–191.

———, 1962, Mechanics of deformation and acoustic propagation in porous media: Journal of Applied Physics, **33**, 1482–1498.

Bonnet, E., O. Bour, N. E. Odling, P. Davy, I. Main, P. Cowie, and B. Berkowitz, 2001, Scaling of fracture systems in geological media: Reviews of Geophysics, **39**, 347–383.

Bourbié, T., O. Coussy, and B. Zinszner, 1987, Acoustics of porous media: Editions TECHNIP.

Buchen, P., and R. Ben-Hador, 1996, Free-mode surface-wave computations: Geophysical Journal International, **124**, 869–887.

Caspari, E., M. Milani, J. G. Rubino, T. M. Müller, B. Quintal, and K. Holliger, 2016, Numerical upscaling of frequency-dependent P-and S-wave moduli in fractured porous media: Geophysical Prospecting, **64**, 1166–1179.

Chen, Y.-F., S. Fang, D.-S. Wu, and R. Hu, 2017, Visualizing and quantifying the crossover from capillary fingering to viscous fingering in a rough fracture: Water Resources Research, **53**, 7756–7772.

de Dreuzy, J.-R., P. Davy, and O. Bour, 2001, Hydraulic properties of two-dimensional random fracture networks following a power law length distribution: 1. Effective connectivity: Water Resources Research, **37**, 2065–2078.

Detournay, E., and A. H.-D. Cheng, 1993, Fundamentals of poroelasticity, *in* Analysis and design methods: Pergamon, 113–171.

Dvorkin, J., M. A. Gutierrez, and D. Grana, 2014, Seismic reflections of rock properties: Cambridge University Press.

Fatti, J. L., G. C. Smith, P. J. Vail, P. J. Strauss, and P. R. Levitt, 1994, Detection of gas in sandstone reservoirs using avo analysis: A 3-d seismic case history using the geostack technique: Geophysics, **59**, 1362–1376.

Favino, M., J. Hunziker, E. Caspari, B. Quintal, K. Holliger, and R. Krause, 2020, Fully-automated adaptive mesh refinement for media embedding complex heterogeneities: application to poroelastic fluid pressure diffusion: Computational Geosciences, **24**, 1101–1120.

Glass, R. J., M. J. Nicholl, H. Rajaram, and B. Andre, 2004, Development of slender transport pathways in unsaturated fractured rock: Simulation with modified invasion percolation: Geophysical research letters, **31**.

Grab, M., B. Quintal, E. Caspari, C. Deuber, H. Maurer, and S. Greenhalgh, 2017, The effect of boiling on seismic properties of water-saturated fractured rock: Journal of Geophysical Research: Solid Earth, **122**, 9228–9252.

Gunasekera, R. C., G. R. Foulger, and B. R. Julian, 2003, Reservoir depletion at the geysers geothermal area, california, shown by four-dimensional seismic tomography: Journal of Geophysical Research: Solid Earth, **108**.

Gurevich, B., M. Brajanovski, R. J. Galvin, T. M. Müller, and J. Toms-Stewart, 2009, P-wave dispersion and attenuation in fractured and porous reservoirs–poroelasticity approach: Geophysical Prospecting, **57**, 225–237.

Hall, Matt; Dramsch, J., 2015, Reflection.py: https://github.com/ agilescientific/ bruges/ blob/ main/ bruges/ reflection/ reflection.py, accessed July, **18**, 2022.

He, Y., J. G. Rubino, S. G. Solazzi, N. D. Barbosa, M. Favino, T. Chen, J. Gao, and K. Holliger, 2022, Numerical upscaling of seismic signatures of poroelastic rocks containing mesoscopic fluid-saturated voids: Journal of Geophysical Research: Solid Earth, **127**, e2021JB023473.

Holmgren, M., 2006, X steam for matlab: www.x-eng.com, accessed June, **21**, 2022.

Hu, R., C.-X. Zhou, D.-S. Wu, Z. Yang, and Y.-F. Chen, 2019, Roughness control on multiphase flow in rock fractures: Geophysical Research Letters, **46**, 12002–12011.

Hunziker, J., M. Favino, E. Caspari, B. Quintal, J. G. Rubino, R. Krause, and K. Holliger, 2018, Seismic attenuation and stiffness modulus dispersion in porous rocks containing stochastic fracture networks: Journal of Geophysical Research: Solid Earth, **123**, 125–143.

Kazemeini, S. H., C. Juhlin, and S. Fomel, 2010, Monitoring CO_2 response on surface seismic data; a rock physics and seismic modeling feasibility study at the CO_2 sequestration site, Ketzin, Germany: Journal of Applied Geophysics, **71**, 109–124.

Kong, L., B. Gurevich, T. M. Müller, Y. Wang, and H. Yang, 2013, Effect of fracture fill on seismic attenuation and dispersion in fractured porous rocks: Geophysical Journal International, **195**, 1679–1688.

Lei, Q., and D. Sornette, 2021, Transport and localization of elastic waves in two-dimensional fractured media: Consequences on scattering attenuation: Journal of Geophysical Research: Solid Earth, **126**, e2020JB021178.

Lissa, S., N. D. Barbosa, and B. Quintal, 2021, Fluid pressure diffusion in fractured media: the role played by the geometry of real fractures: Journal of Geophysical Research: Solid Earth, **126**, e2021JB022233.

Masson, Y. J., and S. R. Pride, 2007, Poroelastic finite difference modeling of seismic attenuation and dispersion due to mesoscopic-scale heterogeneity: Journal of Geophysical Research: Solid Earth, **112**.

Mavko, G., T. Mukerji, and J. Dvorkin, 1998, The Rock Physics Handbook: Cambridge University Press.

Milani, M., J. G. Rubino, T. M. Müller, B. Quintal, E. Caspari, and K. Holliger, 2016, Representative elementary volumes for evaluating effective seismic properties of heterogeneous poroelastic media: Geophysics, **81**, D169–D181.

Nakagawa, S., and M. A. Schoenberg, 2007, Poroelastic modeling of seismic boundary conditions across a fracture: The Journal of the Acoustical Society of America, **122**, 831–847.

Obermann, A., T. Kraft, E. Larose, and S. Wiemer, 2015, Potential of ambient seismic noise techniques to monitor the St. Gallen geothermal site (Switzerland): Journal of Geophysical Research: Solid Earth, **120**, 4301–4316.

Quiroga, G. E., J. G. Rubino, S. G. Solazzi, N. D. Barbosa, and K. Holliger, 2022, Effects of fracture connectivity on rayleigh wave dispersion: Journal of Geophysical Research: Solid Earth, e2021JB022847.

Quiroga, G. E., A. P. K. Ziyisyian, and F. Späth, 2018, AVO inversion on unconventional reservoirs: systematic estimation of uncertainty in the Vaca Muerta shale: First Break, **36**, 65–74.

Roach, L. A., D. J. White, and B. Roberts, 2015, Assessment of 4D seismic repeatability and CO2 detection limits using a sparse permanent land array at the Aquistore CO2 storage site: Geophysics, **80**, WA1–WA13.

Rubino, J. G., E. Caspari, T. M. Müller, and K. Holliger, 2017, Fracture connectivity can reduce the velocity anisotropy of seismic waves: Geophysical Journal International, **210**, 223–227.

Rubino, J. G., E. Caspari, T. M. Müller, M. Milani, N. D. Barbosa, and K. Holliger, 2016, Numerical upscaling in 2-D heterogeneous poroelastic rocks: Anisotropic attenuation and dispersion of seismic waves: Journal of Geophysical Research: Solid Earth, **121**, 6698–6721.

Rubino, J. G., L. Guarracino, T. M. Müller, and K. Holliger, 2013, Do seismic waves sense fracture connectivity?: Geophysical Research Letters, **40**, 692–696.

Rubino, J. G., T. M. Müller, L. Guarracino, M. Milani, and K. Holliger, 2014, Seismoacoustic signatures of fracture connectivity: Journal of Geophysical Research: Solid Earth, **119**, 2252–2271.

Rubino, J. G., C. L. Ravazzoli, and J. E. Santos, 2009, Equivalent viscoelastic solids for heterogeneous fluid-saturated porous rocks: Geophysics, **74**, N1–N13.

Sánchez-Pastor, P., A. Obermann, T. Reinsch, T. Ágústsdóttir, G. Gunnarsson, S. Tómasdóttir, V. Hjörleifsdóttir, G. Hersir, K. Ágústsson, and S. Wiemer, 2021, Imaging high-temperature geothermal reservoirs with ambient seismic noise tomography, a case study of the Hengill geothermal field, SW Iceland: Geothermics, **96**, 102207.

Scott, S. W., 2020, Decompression boiling and natural steam cap formation in high-enthalpy geothermal systems: Journal of Volcanology and Geothermal Research, **395**, 106765.

Shuey, R., 1985, A simplification of the Zoeppritz equations: Geophysics, **50**, 609–614.

Solazzi, S. G., J. Hunziker, E. Caspari, J. G. Rubino, M. Favino, and K. Holliger, 2020, Seismic signatures of fractured porous rocks: the partially saturated case: Journal of Geophysical Research: Solid Earth, **125**, e2020JB019960.

Solazzi, S. G., S. Lissa, J. G. Rubino, and K. Holliger, 2021, Squirt flow in partially saturated cracks: a simple analytical model: Geophysical Journal International, **227**, 680–692.

Solazzi, S. G., J. Rubino, T. M. Müller, M. Milani, L. Guarracino, and K. Holliger, 2016, An energy-based approach to estimate seismic attenuation due to wave-induced fluid flow in heterogeneous poroelastic media: Geophysical Journal International, **207**, 823–832.

Stork, A. L., C. Allmark, A. Curtis, J.-M. Kendall, and D. J. White, 2018, Assessing the potential to use repeated ambient noise seismic tomography to detect CO_2 leaks: Application to the Aquistore storage site: International Journal of Greenhouse Gas Control, **71**, 20–35.

Taira, T., A. Nayak, F. Brenguier, and M. Manga, 2018, Monitoring reservoir response to earthquakes and fluid extraction, Salton Sea geothermal field, California: Science Advances, **4**, e1701536.

Thomas, M., V. Ball, J. Blangy, and L. Tenorio, 2016, Rock-physics relationships between inverted elastic reflectivities: The Leading Edge, **35**, 438–444.

Tiab, D., and E. C. Donaldson, 2015, Petrophysics: theory and practice of measuring reservoir rock and fluid transport properties: Gulf professional publishing.

Toledo, T., A. Obermann, A. Verdel, J. Martins, P. Jousset, A. Mortensen, K. Erbas, and C. Krawczyk, 2022, Ambient seismic noise monitoring and imaging at the Theistareykir geothermal field (Iceland): Journal of Volcanology and Geothermal Research, 107590.

Vermilye, J. M., and C. H. Scholz, 1995, Relation between vein length and aperture: Journal of Structural Geology, **17**, 423–434.

Vinci, C., J. Renner, and H. Steeb, 2014, On attenuation of seismic waves associated with flow in fractures: Geophysical Research Letters, **41**, 7515–7523.

LIST OF FIGURES

3 (a, b, c) P- and (d, e, f) S-wave velocities as functions of frequency for a single realization of connected (dotted lines) and unconnected (dashed lines) fracture networks. Steam saturation of the fractures S_s^f is (a, d) 0%, (b, e) 50% and (c, f) 100%.

4 (a, b, c) P- and (d, e, f) S-wave velocities as functions of steam saturation S_s^f for different fracture connectivity scenarios. Blue lines correspond to the elastic high-frequency limit and red lines to seismic frequencies within the non-dispersive plateau. The relative velocity change for each connectivity level (g, h, i) is computed as $\Delta V = \frac{V_{P,S}(S_s^f) - V_{P,S}(S_s^f=0)}{V_{P,S}(S_s^f=0)}$, and is shown for V_P (continuous lines) and V_S (dashed lines).

5 (a) Crossplot of V_P/V_S against V_P. Orange dots correspond to randomly connected fracture networks with a fixed fracture density Fd of 1% and varying S_s^f, from 0 to 100%. Blue dots were taken from Quiroga et al. (2022) and correspond to fracture networks with identical fracture properties, varying fracture density from 0.25% to 0.9% and water (K_f = 2250 GPa, $\eta = 1e^{-3}$ Pa.s) as the saturating fluid. V_P values are normalized with respect to the respective maximum values for ease of comparison. V_P-values for variable fracture density are divided by the value of V_P for $Fd = 0.25\%$ and the V_P-values for variable fracture steam saturation by the value of V_P for $S_s^f = 0\%$. (b) V_P/V_S ratio as a function of Fd for fracture networks with full water saturation. (c) V_P/V_S ratio as a function of S_s^f for fracture networks with fracture density $F_d = 1\%$.

6 Schematic representation of the geothermal reservoir model employed in the analysis. The sandstone and intact granitic layers are considered to be homogeneous,

while the granitic reservoir is characterized as a fractured formation with the fractures being saturated with either water and steam (upper part of the reservoir) and only water (lower part of the reservoir).

7 (a, b) Phase and group velocity dispersion of Rayleigh waves for the model described in Table 3 for different levels of steam saturation in the upper part of the reservoir, considering (a) a poroelastic and (b) an elastic approach. Relative velocity difference ($\Delta V_p, g(S_s^f)$) for phase (solid lines) and group velocities (dashed lines) for (c) poroelastic and (d) elastic approaches. Relative velocity differences are computed as the maximum difference between the dispersion at a certain steam saturation and the dispersion corresponding to a steam saturation of 0% divided by the value of the latter.

8 P-wave reflection coefficient and AVA coefficients for the interface between the partially steam-saturated upper part of the reservoir and the water-saturated lower part of the reservoir. (a) Reflectivity as a function of angle and S_s^f (100% red, 50% yellow, and 10% blue) for poroelastic (continuous lines) and elastic approaches (dashed lines). Results for the inversion using (b) Shuey's and (c) Fatti's approximations for incidence angles between 0° and 50°. Inversion results are shown for the poroelastic (dots) and for elastic (crosses) approaches.

9 P-wave reflection coefficient as a function of incidence angle for the interfaces between: a partially steam-saturated upper part of the reservoir and a fully water-saturated lower part of the reservoir (solid lines); a fully water-saturated upper part of the reservoir with varying fracture density Fd over a fully water-saturated lower part of the reservoir with a Fd=0.25% (dashed lines). Results for the inversion using

(b) Shuey's and (c) Fatti's approximations for incidence angles between 0 and 50°. Inversion results are shown for both variable S_s^f (dots) and the variable Fd scenarios (stars).

B-1 Standard deviations of (a, c, e) P- and (b, d, f) S-wave velocities for the non-dispersive plateau as functions of the number of realizations for (a, b) connected, (c, d) unconnected, and (e, f) randomly connected samples. Colors denote the percentage of steam saturation of the fractures for each series of realizations.

LIST OF TABLES